Asian Journal of Chemistry; Vol. 37, No. 8 (2025), 2031-2036

ASIAN JOURNAL OF CHEMISTRY

https://doi.org/10.14233/ajchem.2025.34062

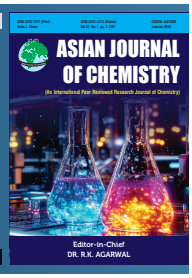

Crystal Structure Analysis, Cationic and Magnetic Studies of Cobalt Ferrite Nanoparticles

SUDARSHAN GAWALI[1,*], PRATIK S. PATIL[1], YOGESH P. UBALE[1], VISHNU SURASHE[2] and K.M. JADHAV[1,3]

[1]Department of Physics, Dr. Babasaheb Ambedkar Marathwada Universitiy, Chhatrapati Sambhajinagar-431004, India
[2]Department of Physics, Arts, Science and Commerce College, Badnapur-431202, India
[3]Department of Physics, School of Basic and Applied Sciences, MGM University, Chhatrapati Sambhajinagar-431001, India

*Corresponding author: E-mail: ssgawali3@gmail.com

Received: 16 May 2025; *Accepted*: 22 July 2025; *Published online*: 31 July 2025; AJC-22082

In present study, we focus on the synthesis of cobalt ferrite ($CoFe_2O_4$) magnetic nanoparticles *via* wet chemical sol-gel self-ignition method using black pepper (*Piper nigrum*) as a fuel. The X-ray diffraction (XRD) investigations verified the mono-phase evolution of the simple cubic FCC type spinel structure. The crystal structure parameters, such as lattice constant (a = 8.386 Å), lattice strain, microstrain, stacking fault, *etc*. are obtained from XRD data and making use of the Williamson-Hall (W-H) plot. The Debye-Scherrer's formula estimated crystallite size to be approximately 22.53 nm. The results of cation distribution suggest that cobalt ferrite have spinel structure with inverse nature. FTIR spectrum shows the two prominent absorption bands within 400 to 600 cm^{-1} range. The morphological study shows the spherical nature of the particle with a grain size of 14 ± 2.01 nm. Raman spectra reveal the Raman modes, *viz*. ($A_{1g} + E_g + 3T_{2g}$). Enhancement in saturation magnetization and decrement in coercivity were observed through the M-H curve.

Keywords: Cobalt ferrite, *Piper nigrum*, Crystal structure, Morphology, Magnetic properties.

INTRODUCTION

Magnetic oxide systems, such as ferrites, have been of considerable interest to many researchers in the past owing to tunable properties. The main constituents of ferrite are iron oxide (Fe_2O_3) and metal oxide (MO), which may be divalent metal ions like Co, Ni, Zn, *etc*. or rare earth ions like Gd, Dy, Y, *etc*. or large divalent ions like Ba, Ca, Sr, *etc*. [1-3]. The crystal structure of ferrite emerges into three groups, namely spinel ferrite, garnet and hexagonal ferrite.

Ferrite exhibits magnetic properties like saturation magnetization, coercivity and remanence magnetization [4]. On the basis of coercivity values, ferrites are of two types *viz*. soft ferrite and rigid ferrite [5]. Ferrites with coercivity less than 1000 Oe are known as soft ferrites [6], while those with coercivity greater than 1000 Oe are known as hard ferrites [7]. Several researchers have extensively studied spinel ferrite, which belongs to the soft ferrite category [8]. Rare earth garnet and hexagonal ferrite belong to the hard ferrite [9]. The important features of spinel ferrite include high electrical resistance, low energy loss from eddy currents, strong magnetization, high permeability, strong magneto-crystalline anisotropy, low dielectric constant, moderate band gap, ability to conduct electricity and compatibility with living tissues [10-13]. The mentioned features of spinel ferrite are of interest from the point of view of their applications.

Spinel ferrites are used in transformer cores [14], antenna rods [15], sensors [16], magnetic data storage [17], telecommunications [18], *etc*., due of its better electrical, dielectric [19], optical and magnetic properties [20]. Many researchers have investigated the electrical resistivity dielectric constant, saturation magnetization, coercivity of spinel ferrite for various applications [21]. The properties of spinel ferrites differ between bulk and nano-sized forms. The nano-sized ferrite shows excellent properties such as a smaller size of the order of 10^{-9} m, chemical stability, greater reactivity at the atomic and molecular level, a large surface-to-volume ratio, less toxicity, biocompatibility, reusability, *etc*. Synthesis procedure, cations occupancies, their nature, *etc*. affects the features of nanocrystalline spinel ferrites [22-25].

In nanotechnology, the bottom-up approach and the top-down approach are used to synthesize nanomaterials. Ball

This is an open access journal, and articles are distributed under the terms of the Attribution 4.0 International (CC BY 4.0) License. This license lets others distribute, remix, tweak, and build upon your work, even commercially, as long as they credit the author for the original creation. You must give appropriate credit, provide a link to the license, and indicate if changes were made.

milling, thermal evaporation, laser ablation, sputtering, *etc*. belong to the top-down approach [26]. The low temperature solution-based techniques like chemical co-precipitation, sol-gel synthesis, hydrothermal, microemulsion, *etc*. belong to the bottom-up approach [27]. Among these methods, sol-gel auto-combustion synthesis are of significant interest to several researchers. These method uses nitrates as a reagent and citric acid, glycine, dextrose, *etc*. as a fuel/chelating agent. At the same time, the method has some drawbacks, like the evolution of toxic gases [28]. Hence, in recent years, the green synthesis approach has been developed to reduce the evolution of toxic gases. The green method mostly uses the extract of the plants, fungi, algae, *etc*. as a source of fuel [29]. The use of biogenic fuel not only helps in reducing the toxic gases but also influences the morphology of the nanoparticles [30].

In addition to the method of preparation, the cation distribution is also important and strongly influences the crystal structure, microstructural and ferromagnetic properties of spinel ferrite. X-ray diffraction and neutron diffraction are the most powerful techniques to probe the cationic arrangement [31,32]. In light of above facts, it is decided to prepare $CoFe_2O_4$ ferrite with nanosize by sol-gel self-ignition technique to study the crystal structure, cation distribution, infrared, Raman, morphological and magnetic properties using standard techniques.

EXPERIMENTAL

AR grade hydrated cobalt nitrate and hydrated ferric nitrate having the chemical formula ($Co(NO_3)_2{\cdot}6H_2O$) and ($Fe(NO_3)_3{\cdot}9H_2O$), respectively were used as a raw material for the synthesis of cobalt ferrite nanoparticles. Ammonia was used to maintain the pH of the mixed nitrate solution and citric acid was used as a fuel.

General procedure: In this work, the synthesis of cobalt ferrite ($CoFe_2O_4$) magnetic nanoparticles was carried out by using a green and eco-friendly route involving black pepper extract instead of conventional citric acid. Initially, cobalt and ferric salts dissolved in deionized water and were mixed together, followed by the addition of black pepper extract, which acts as a natural reducing and stabilizing agent. The resulting mixture forms a clear solution and to maintain the neutral pH and facilitate further reactions, ammonia solution was added until the pH reaches around 7. And then the solution was continuously agitated at 80 ºC, which led to the formation of sol and later, a viscous gel. The gel was further heated above 100 ºC for 0.5 h. At this temperature, the gel self-ignited producing large heat for few seconds and converting into ash. This resultant ash like powder is a desired product.

Detection methods: The XRD method was employed to examine the crystalline characteristics and phase pure formation. The crystallographic parameters were analyzed using an Ultima IV X-ray diffractometer from Rigaku Ultima IV, Japan. The X-ray diffraction patterns were measured over a 2θ range from 10º to 80º, utilizing Cu*K*α radiation. Fourier-transform infrared (FTIR) spectrum was measured in the range from 400 to 4000 cm^{-1} at ambient temperature. The field emission scanning electron microscopy (FESEM) technique was used to study the surface morphology. The presence of the elements in sample was evaluated through energy dispersive X-ray analysis (Carl Zeiss Sigma field 300 microscope using an airlock chamber, Cambridge, UK). An X-ray Omicron ESCA, produced by Oxford Instrument Germany, was employed to record the data *via* photoelectron spectroscopy (XPS). Raman spectra were taken with an Invia Confocal Raman microscope (Renishaw Gloucestershire, GL12 8JR, UK) using a 785 nm light source with a power of 1 mW and 10 measurements. The VSM technique was employed to evaluate various magnetic parameters temperature using PPMS system (quantum design) at room temperature.

RESULTS AND DISCUSSION

X-ray diffraction: The X-ray diffraction (XRD) pattern was taken from 10º to 80º at 300 K. The XRD pattern (Fig. 1) shows the diffraction peaks oriented at Bragg angles 30.10º, 35.47º, 37.07º, 43.12º, 53.53º, 57.05º and 62.65º, which are related to (220), (311), (222), (400), (422), (511) and (440), respectively. The intense and slightly broader diffraction peaks correspond to a simple cubic structure. The XRD pattern revealed no additional peaks beyond the cubic phase, thereby confirming the single-phase crystal structure and also closely matches JCPDS card no. 22-1086 [33]. The Scherrer equation was applied to estimate the crystallite size, with the (311) peak displaying the maximum intensity [34].

$$t = \frac{K\lambda}{\beta\cos\theta} \quad (1)$$

where notations have their usual meaning.

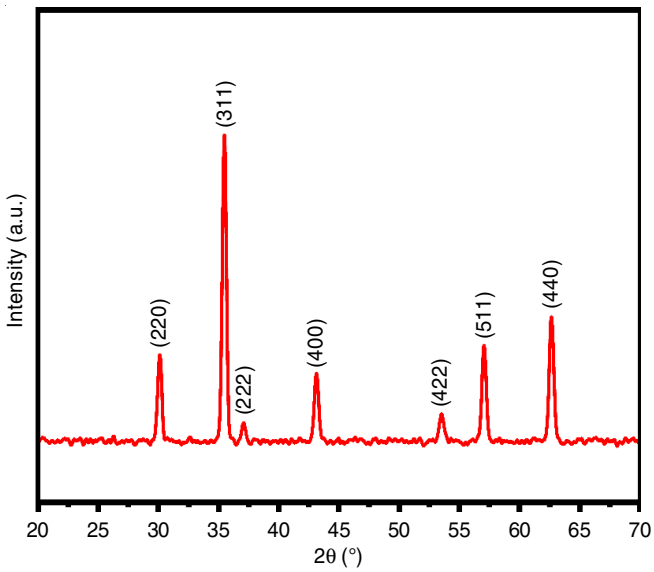

Fig. 1. XRD spectrum for $CoFe_2O_4$ nanoparticles

Based on the above equation, the crystallite size of approximately 22.528 nm.

Lattice constant (a): The crystal structure parameter lattice constant (a) can be obtained using eqn. 2 [35]:

$$\alpha = d{\cdot}\sqrt{h^2 + k^2 + l^2} \quad (2)$$

where d is used to represent the interplanar spacing and (*h k l*) represents the Miller indices.

The lattice constant calculated from the above relation is found to be of the order of 8.386 Å, which is in close agreement with the literature values [36]. Using the lattice constant values, the unit cell volume V was also calculated and is obtained to be 589.784 Å^3.

The other crystal structure parameters, X-ray density was also estimated by using eqn. 3 [35]:

$$d_x = \frac{Z \times M}{V \times N_A} \quad (3)$$

where notations have their usual meaning.

The X-ray density is inversely proportional to the lattice constant. All the determined values of crystallite size, lattice constant, *etc*. standard parameters are tabulated in Table-1.

TABLE-1
VALUES OF CRYSTALLITE SIZE (t) (nm), LATTICE CONSTANT (a) (Å), X-RAY DENSITY (d_X) (g/cc) AND UNIT CELL VOLUME (V) (Å^3) FOR $CoFe_2O_4$ NANOPARTICLES

Sample	t (nm)	a (Å)	d_x (g/cm^3)	V (Å^3)
$CoFe_2O_4$	22.53	8.386	5.285	589.784
$CoFe_2O_4$ [37]	26	8.389	4.650	590.38

Williamson-Hall (W-H) plot: The Williamson-Hall (W-H) plot is dependent on the size and strain broadening. Fig. 2 depicts the W-H plot of the present cobalt ferrite nanoparticles. The plot exhibits a straight line and follows the equation [38]:

$$\beta_{hkl} = 4\sin\theta + \frac{k\lambda}{D_{W-H}} \quad (4)$$

where notations have their usual meaning.

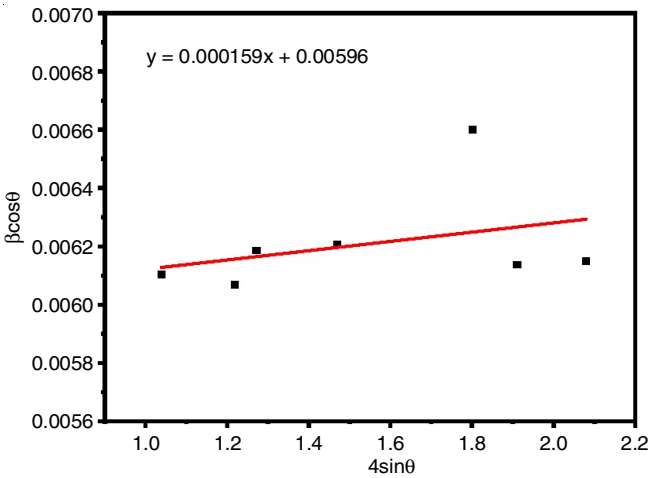

Fig. 2. W-H plot for $CoFe_2O_4$ nanoparticles

The slope of the plot gives the value of microstrain (ε) and the extrapolated intercept on the y-axis gives the crystallite size. The obtained value is similar to that reported in the literature [39].

Dislocation density: The dislocation density is the number of dislocations per unit volume or per unit area in a material, essentially measuring the concentration of these lattice defects. The dislocation density is defined by using eqn. 5 [40]:

$$\delta = \frac{1}{D^2} \quad (5)$$

Stacking fault: The other microstructural parameter stacking fault (SF) was also determined and is considered as a planar defect in a crystal structure in which the regular stacking sequence of atomic layers is disturbed, resulting in a local error in the crystal lattice [40].

$$SF = \frac{2\pi^2}{45\sqrt{3\tan\theta}} \quad (6)$$

Lattice strain: Lattice strain (LS) refers to the deviation of a crystal lattice from its ideal, unstrained state due to the imperfections like dislocations or variations in atomic spacing [40].

$$LS = \frac{\beta}{4\tan\theta} \quad (7)$$

The obtained values of micro-strain, stacking fault, dislocation density and lattice strain are given in Table-2 and are agreed fairly well with the literature values [40].

Cation distribution: The crystal structure parameters and various magnetic characteristics such as saturation magnetization, coercivity, *etc*. are sensitive to the arrangement of cations located at [A] site and [B] site. The X-ray diffraction method is applied to study the cation distribution of cobalt ferrite nanoparticles. The method is based on the comparison of observed X-ray intensity ratio and calculated intensity ratio for a given (*hkl*). The Burger's formula (eqn. 8) was used to estimate the X-ray intensity (I) [43]:

$$I_{hkl} = |hkl|^2 P * L_p \quad (8)$$

where notations have their usual meaning [43]. The L_p is given by eqn. 9:

$$L_P = \frac{1+\cos^2 2\theta}{\sin^2\theta\cos\theta} \quad (9)$$

Intensity was calculated for various possible arrangements of cations in [A] site and [B] site (Table-3). The calculated intensity ratio is compared with the observed intensity ratio. The close agreement between observed intensity ratio and calculated intensity ratio for a given distribution of cations is assumed to be the possible cation distribution. The results of cation distribution are mentioned in Table-4.

FTIR: Fig. 3 illustrates the FTIR of prepared cobalt ferrite nanoparticles measured in the 4000-400 cm^{-1} region. The two

TABLE-2
VALUES FOR MICROSTRUCTURAL PARAMETERS LIKE DISLOCATION DENSITY (δ) (lines/m^2), LATTICE STRAIN (LS), STACKING FAULT (SF), MICRO STRAIN (ε) AND CRYSTALLITE SIZE FROM W-H PLOT (t_{W-H}) (nm) FOR $CoFe_2O_4$ NANOPARTICLES

Sample	δ (lines/m^2)	LS	SF	ε	t_{W-H} (nm)
$CoFe_2O_4$	19.7×10^{14}	4.98×10^{-3}	0.4480	1.59×10^{-4}	23.26
$CoFe_2O_4$ [41,42]	7.82×10^{14}	5.00×10^{-3}	0.40	5.60×10^{-4}	19

TABLE-3
VALUES OF MILLER INDICES PLANE (*hkl*), OBSERVED AND CALCULATED INTENSITY, POLARIZATION (P), LORENTZ POLARIZATION FACTOR L_p FOR $CoFe_2O_4$ NANOPARTICLES

2θ (°)	Plane (h k l)	I (Obs.)	I (Calc.)	P	L_p
43.12	(400)	2719.109	10394900	6	12.202
53.53	(422)	1252.467	455625.85	24	7.474

TABLE-4
CATION DISTRIBUTION, INTENSITY RATIOS (OBSERVED AND CALCULATED) FOR $CoFe_2O_4$ NANOPARTICLES

Site [A]	Site [B]	$\frac{I_{(422)}(Obs.)}{I_{(400)}(Obs.)}$	$\frac{I_{(422)}(Cal.)}{I_{(400)}(Cal.)}$
(Fe)	[CoFe]	0.2506	0.4606

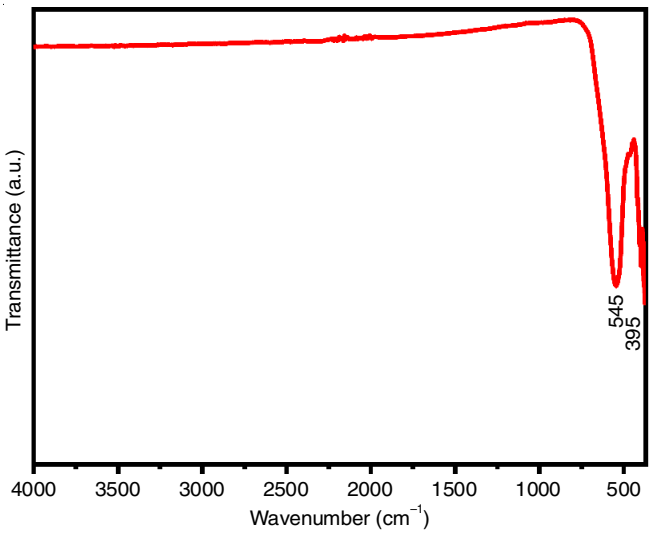

Fig. 3. FTIR spectra for $CoFe_2O_4$ nanoparticles

absorption bands at 545 cm^{-1} and 395 cm^{-1} are observed, which characterize the spinel structure. According to Waldrone's analysis, the high-frequency band ν_1 is assigned to the intrinsic vibrations of the tetrahedral [A] site and the low-frequency band is attributed to the intrinsic vibration of octahedral [B] site. Similar absorption bands are observed in other spinel ferrites. The values of band frequencies ν_1 and ν_2 are given in Table-5 and are used to calculate the force constants K_t and K_o using the standard relation (eqn. 11):

TABLE-5
VALUES OF INFRARED VIBRATIONAL MODES (ν_1 AND ν_2), FORCE CONSTANTS (K_t AND k_o) FOR $CoFe_2O_4$ NANOPARTICLES

Composition (x)	ν_1 (cm^{-1})	ν_2 (cm^{-1})	k_t (N/m)	k_o (N/m)
$CoFe_2O_4$	545	395	217.94	129.26
$CoFe_2O_4$ [44]	611	434	1.810*10^2	96.10

$$k = 4\pi^2 c^2 \nu^2 \mu^2 \text{ N/m} \quad (11)$$

To calculate the force constant (k), the cation distribution given in Table-4 is also used. The obtained values of the force constants are given in Table-5 and are in good agreement with the values reported in the literature.

Morphological studies: Fig. 4 illustrates the surface morphology, particle size distribution, and elemental composition of the synthesized cobalt ferrite ($CoFe_2O_4$) nanoparticles. The FESEM micrograph shows that the $CoFe_2O_4$ nanoparticles have a somewhat agglomerated, roughly spherical shape, which is typical of ferrite nanoparticles because of their high surface energy and magnetic interactions. With no notable irregularities or sizable clusters, the particles seem to be evenly dispersed, suggesting a rather regulated synthesis process. Based on many measurements of the particles in the FESEM picture, the particle size distribution histogram reveals that the bulk of the particles lie within a small size window, having average particle size of 15 nm. This indicates high homogeneity and validates that the synthesized cobalt ferrite is nanoscale. The EDX spectrum provides additional evidence of the sample's elemental content. Strong peaks that represent iron (Fe), cobalt (Co) and oxygen (O) are seen, confirming that $CoFe_2O_4$ was successfully formed. Other notable elemental peaks are absent, indicating that the produced nanoparticles are highly pure.

Raman spectroscopy: Synthesized $CoFe_2O_4$ spinel ferrite nanoparticles have Raman modes at 297.33 cm^{-1}, 468.19 cm^{-1}, 560.37 cm^{-1}, 610.75 cm^{-1} and 690.99 cm^{-1}, as shown in Fig. 5. According to group theory analysis, $5T_{1u} + A_{1g} + E_g + 3T_{2g}$ modes can be found [45], with the $^5T_{1u}$ modes being IR active and the other five ($A_{1g} + E_g + 3T_{2g}$) modes being Raman active, consisting of O ion mobility and both A-site and B-site ions in the spinel structure. The A_{1g}, E_g and T_{2g} models correspond to the symmetric stretching of O^{2-} ions, symmetric bending of O^{2-} ion and asymmetric stretching of O^{2-} ions, respectively.

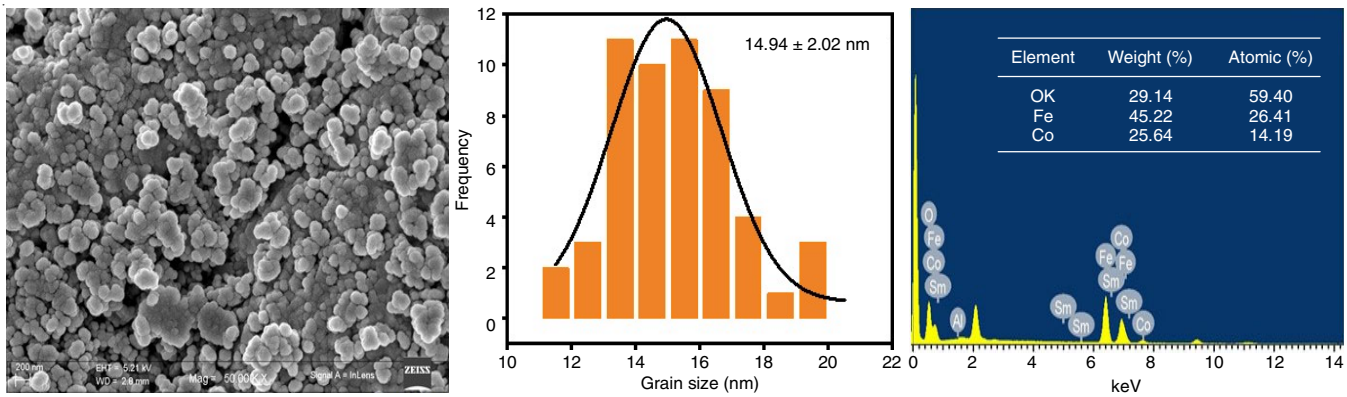

Fig. 4. FE-SEM image, histogram and EDX spectra of $CoFe_2O_4$ nanoparticles

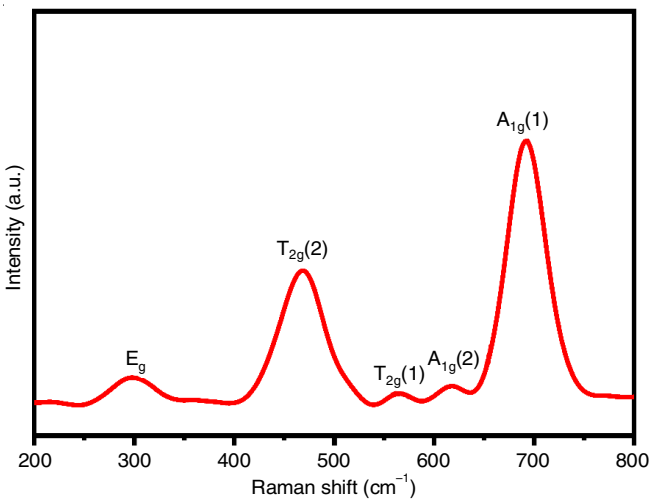

Fig. 5. Raman spectra for $CoFe_2O_4$ nanoparticles

Furthermore, the symmetric stretching of the oxygen anion is associated with the A_{1g} mode, symmetric bending with the E_g mode and asymmetric stretching with respect to the tetrahedral and octahedral cations with the T_{2g} mode [46].

Vibrating sample magnetometer: Fig. 6 depicts the plot of saturation magnetization against applied magnetic field for cobalt ferrite ($CoFe_2O_4$) nanoparticles at ambient temperature. The observed magneton number was calculated using eqn. 12 [47]:

$$n_B = \frac{M * M_s}{5585} \quad (12)$$

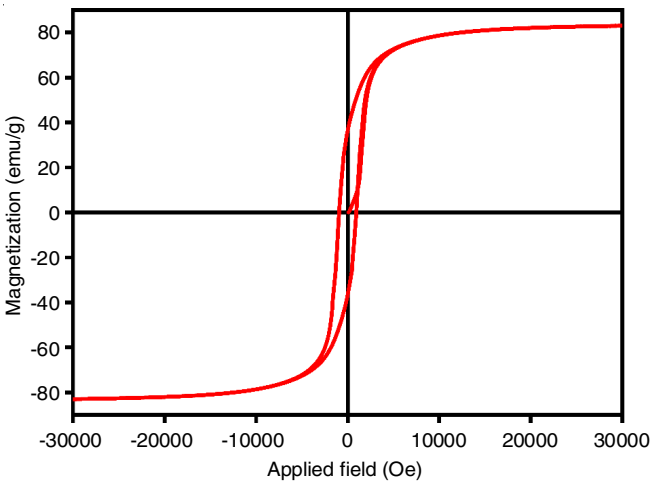

Fig. 6. VSM plot for $CoFe_2O_4$ nanoparticles

The Neel's magnetic moment was also calculated using the relation given below [48]:

$$n_B^N = M_B - M_A \quad (13)$$

To determine M_B and M_A, the distribution of cations and the magnetic moments of Fe^{3+} and Co^{2+}, which are 5 μB and 3 μB, respectively and the values are tabulated in Table-6.

In certain ferromagnetism materials, the magnetization curve does not intersect the origin; rather, it generates a loop representing magnetization in response to an applied magnetic field (M-H). Since the M-H loops do not pass through the origin, they maintain a magnetization value at zero applied magnetic field, which is known as remnant magnetization (M_r). The anisotropic constant K was determined by following the relation and their values are given in Table-6. It is seen that the anisotropic constant decreases with decrease in coercivity.

$$K = \frac{H_c * M_s}{0.98} \quad (14)$$

Conclusion

The sol-gel synthesis approach has been successfully employed to prepare the cobalt ferrite nanoparticles in a single phase using black pepper (*Piper nigrum*) extract as green fuel which also acts as a cheleting agent.The crystal structure is FCC type cubic structure.The lattice constant and several other structural parameters are also evaluated to gain deeper insights into the prepared material's characteristics. FTIR analysis confirmed the formation of spinel ferrite nanoparticles in pure form. Raman spectrum with five active modes reveals the formation of cobalt ferrite nanoparticles. Surface studies through FESEM reveal a grain-like structure with a grain size of 14 ± 2.02 nm. EDX analysis suggests the presence of all the ions in stoichiometric proportion. The M-H plots exhibit enhancement in magnetization and decrement in coercivity as compared to the bulk ferrite. The inverse spinel structure was confirmed through cation distribution studies.

ACKNOWLEDGEMENTS

One of the authors, S.S. Gawali, is thankful to Punyashlok Ahilyadevi Holkar Solapur University, Solapur and TIFR, Mumbai, Department of Chemistry, Dr. B.A.M. University, Chhatrapati Sambhajinagar, India for conducting the various experimental characterization.

CONFLICT OF INTEREST

The authors declare that there is no conflict of interests regarding the publication of this article.

REFERENCES

1. A. Hao and X. Ning, *Front. Mater.*, **8**, 718869 (2021); https://doi.org/10.3389/fmats.2021.718869
2. K.K. Kefeni, B.B. Mamba and T.A. Msagati, *Sep. Purif. Technol.*, **188**, 399 (2017); https://doi.org/10.1016/j.seppur.2017.07.015

TABLE-6
SATURATION MAGNETIZATION (M_s), REMANENCE MAGNETIZATION (M_r), COERCIVITY (H_c) AND MAGNETON NUMBER (η_B), SQUARENESS RATIO (S_R) OF $CoFe_2O_4$ NANOPARTICLES RECORDED AT ROOM TEMPERATURE

Sample	M_s (emu/g)	M_r (emu/g)	H_c (Oe)	η_B (Obs.) (μ_B)	η_B (Cal.) (μ_B)	S_R	$K \times 10^6$ (erg/cm^3)
$CoFe_2O_4$	83.00	36.58	939.11	3.487	3	0.441	0.64
$CoFe_2O_4$ [49]	75	36	450	2.98	3.40	0.5	0.77

3. O. Dehghani Dastjerdi, H. Shokrollahi and S. Mirshekari, *Inorg. Chem. Commun.*, **153**, 110797 (2023); https://doi.org/10.1016/j.inoche.2023.110797
4. A. Franco Jr. and F.C. e Silva, *Appl. Phys. Lett.*, **96**, 172505 (2010); https://doi.org/10.1063/1.3422478
5. G.K. Bhargava, S. Bhardwaj, M. Singh and K.M. Batoo, Ferrites and Multiferroics: Fundamentals to Applications, Springer Nature (2021).
6. P. Gómez, D. Elduque, C. Pina and C. Javierre, *Materials*, **11**, 1789 (2018); https://doi.org/10.3390/ma11101789
7. H. Jalili, B. Aslibeiki, A.G. Varzaneh V.A. Chernenko, *Beilstein J. Nanotechnol*., **10**, 1348 (2019); https://doi.org/10.3762/bjnano.10.133
8. A. Alhadhrami, M. Zeshan and H.M.T. Farid, *J. Austral. Ceram. Soc.*, **60**, 609 (2024); https://doi.org/10.1007/s41779-023-00982-9
9. A.I. Borhan, D. Gherca, A.R. Iordan and M.N. Palamaru, Classification and Types of Ferrites, In: Ferrite Nanostructured Magnetic Materials, Woodhead Publishing Series in Electronic and Optical Materials, Chap. 2, pp. 17-34 (2023).
10. V.G. Kostishin, I.M. Isaev and D.V. Salogub, *Polymers*, **16**, 1003 (2024); https://doi.org/10.3390/polym16071003
11. A. Manohar, V. Vijayakanth, S.V.P. Vattikuti and K.H. Kim, *Mater. Chem. Phys.*, **286**, 126117 (2022); https://doi.org/10.1016/j.matchemphys.2022.126117
12. S.J. Salih and W.M. Mahmood, *Heliyon*, **9**, e16601 (2023); https://doi.org/10.1016/j.heliyon.2023.e16601
13. S. Sambhudevan, *Chem. Pap.*, **75**, 3697 (2021); https://doi.org/10.1007/s11696-021-01664-1
14. B.S. Ram, A.K. Paul and S. Kulkarni, *J. Magn. Magn. Mater.*, **537**, 168210 (2021); https://doi.org/10.1016/j.jmmm.2021.168210
15. V. Dyo, T. Ajmal, B. Allen, D. Jazani and I. Ivanov, *J. Eng.*, **2013**, 89 (2013); https://doi.org/10.1049/joe.2013.0126
16. A. Šutka and K.A. Gross, *Sens. Actuators B Chem.*, **222**, 95 (2016); https://doi.org/10.1016/j.snb.2015.08.027
17. S. Dubey, S. and A. Vedrtnam, *Invertis J. Sci. Technol.*, **15**, 14 (2022); https://doi.org/10.5958/2454-762X.2022.00003.8
18. S. Kumar and R.R. Singh, in eds.: P. Sharma, G.K. Bhargava, S. Bhardwaj and I. Sharma, Ferrite Nanoparticles for Telecommunication Application, In: Engineered Ferrites and Their Applications, Springer Nature, Singapore, Chap. 6, pp. 95-112 (2023).
19. R.S. Yadav, I. Kuøitka, J. Vilcakova, J. Havlica, J. Masilko, L. Kalina, J. Tkacz, V. Enev and M. Hajdúchová, *J. Phys. Chem. Solids*, **107**, 150 (2017); https://doi.org/10.1016/j.jpcs.2017.04.004
20. M.A. Rafiq, A. Javed, M.N. Rasul, M.A. Khan and A. Hussain, *Ceram. Int.*, **46**, 4976 (2020); https://doi.org/10.1016/j.ceramint.2019.10.237
21. U. Ahmad, M. Afzia, F. Shah, B. Ismail, A. Rahim and R.A. Khan, *Mater. Sci. Semicond. Process.*, **148**, 106830 (2022); https://doi.org/10.1016/j.mssp.2022.106830
22. T.N. Pham, T.Q. Huy and A.-T. Le, *RSC Adv.*, **10**, 31622 (2020); https://doi.org/10.1039/D0RA05133K
23. T. Dippong, E.A. Levei and O. Cadar, *Nanomaterials*, **11**, 1560 (2021); https://doi.org/10.3390/nano11061560
24. S. Chaturvedi and P.N. Dave, *Chem. Methodol.*, **3**, 115 (2019); https://doi.org/10.22034/chemm.2018.143461.1069
25. R. Singh, R. S. Gaur, and R. Kumar, *J. Magn. Magn. Mater*., **503**, 166679 (2020); https://doi.org/10.1016/j.jmmm.2020.166679
26. N. Abid, A.M. Khan, S. Shujait, K. Chaudhary, M. Ikram, M. Imran, J. Haider, M. Khan, Q. Khan and M. Maqbool, *Adv. Colloid Interface Sci.*, **300**, 102597 (2022); https://doi.org/10.1016/j.cis.2021.102597
27. D. Wang, T. Xie and Y. Li, *Nano Res.*, **2**, 30 (2009); https://doi.org/10.1007/s12274-009-9007-x
28. T. Pine, X. Lu, D.R. Mumm, G.S. Samuelsen and J. Brouwer, *J. Am. Cerm. Soc*., **90**, 3735 (2007); https://doi.org/10.1111/j.1551-2916.2007.01919.x
29. S. Ying, Z. Guan, P.C. Ofoegbu, P. Clubb, C. Rico, F. He and J. Hong, *Environ. Technol. Innov.*, **26**, 102336 (2022); https://doi.org/10.1016/j.eti.2022.102336
30. M. Huston, M. DeBella, M. DiBella and A. Gupta, *Nanomaterials*, **11**, 2130 (2021); https://doi.org/10.3390/nano11082130
31. S. Jiao, X. Wang and X. Yu, in eds.: Y. Tang and W. Yao, Neutron Diffraction for Energy Storage Materials, In: Energy Storage Materials Characterization: Determining Properties and Performance, Wiley, Chap. 11, 263 (2025).
32. L. Caselli, L. Conti, I. De Santis and D. Berti, *Adv. Colloid Interface Sci.*, **327**, 103156 (2024); https://doi.org/10.1016/j.cis.2024.103156
33. Y.I. Frantina, F. Fajaroh, Nazriati, Yahmin and Sumari, *AIP Conf. Proc.*, **2330**, 070003 (2021); https://doi.org/10.1063/5.0043377
34. P.S. Patil, S. Bhagat, R. Kokate and K.M. Jadhav, *AIP Conf. Proc.*, **3198**, 020032 (2025); https://doi.org/10.1063/5.0248275
35. P.S. Patil, Y.P. Ubale, S.S. Gawali, M.R. Pai and K.M. Jadhav, *Ceram. Int.*, **50**, 54155 (2024); https://doi.org/10.1016/j.ceramint.2024.10.272
36. B. Boussaida, R. Masrour, Q.Y. Tamboli, S.M. Patange and K.R. Zakde, *Phys. Scr.*, **99**, 115971 (2024); https://doi.org/10.1088/1402-4896/ad8277
37. P. Aghav, V.N. Dhage, M.L. Mane, D.R. Shengule, R.G. Dorik and K.M. Jadhav, *Physica B*, **406**, 4350 (2011); https://doi.org/10.1016/j.physb.2011.08.066
38. S.A. Jadhav, M.V. Khedkar, S.B. Somvanshi and K.M. Jadhav, *Ceram. Int.*, **47**, 28623 (2021); https://doi.org/10.1016/j.ceramint.2021.07.021
39. K.K. Deshmukh, S.P. Nawale, K.A. Gurav, S. Bhagat, A.P. Keche and K.M. Jadhav, *Ceram. Int.*, (2025); https://doi.org/10.1016/j.ceramint.2025.06.043
40. S.Z.H. Hashmi, M. Khalid, G. Mustafa, M.G.B. Ashiq, M. Younas, A. Quddus, H.S.M. Abd-Rabboh, T. Alshahrani, K. Naz and M.M. Javid, *Mater. Chem. Phys.*, **305**, 127912 (2023); https://doi.org/10.1016/j.matchemphys.2023.127912
41. J.P. Singh, J.Y. Park, V. Singh, S.H. Kim, W.C. Lim, H. Kumar, Y.H. Kim, S. Lee and K.H. Chae, *RSC Adv.*, **10**, 21259 (2020); https://doi.org/10.1039/D0RA01653E
42. M. Shobana, G. Nandhini, S. Kavita, V. Suresh Kumar and T. Pazhanivel, *Mater. Sci. Eng. B*, **286**, 116030 (2022); https://doi.org/10.1016/j.mseb.2022.116030
43. B.D. Cullity, Elements of X-ray Diffraction, Addison-Wesley Publishing Company, Inc. (1957).
44. K.V. Chandekar, M. Shkir and S. AlFaify, *J. Mol. Struct.*, **1205**, 127681 (2020); https://doi.org/10.1016/j.molstruc.2020.127681
45. A. Yadav, P. Choudhary, P. Saxena, V.N. Rai and A. Mishra, *J. Adv. Dielectr.*, **9**, 1950014 (2019); https://doi.org/10.1142/S2010135X19500140
46. S.B. Somvanshi, M.V. Khedkar, P.B. Kharat and K.M. Jadhav, *Ceram. Int.*, **46**, 8640 (2020); https://doi.org/10.1016/j.ceramint.2019.12.097
47. Y.P. Ubale, P.S. Patil, S.S. Gawali, S.K. Modi, K.B. Modi and K.M. Jadhav, *J. Supercond. Nov. Magn.*, **38**, 93 (2025); https://doi.org/10.1007/s10948-025-06935-6
48. Y.P. Ubale, P.S. Patil, S.S. Gawali, S.V. Rathod and K.M. Jadhav, *Appl. Phys., A Mater. Sci. Process.*, **131**, 237 (2025); https://doi.org/10.1007/s00339-025-08383-4
49. H. Ghorbani, M. Eshraghi, A.A. Sabouri Dodaran, S. Protasowicki, P. Kameli, C. Johnson and D. Vashaee, *Mater. Res. Bull.*, **147**, 111642 (2022); https://doi.org/10.1016/j.materresbull.2021.111642